Basis Augmentation for High-Order Approximation of Singular Perturbation Problems

Krzysztof J. Fidkowski*
University of Michigan, Ann Arbor, MI, 48188

This paper presents an approximation-space augmentation approach to efficiently resolve singular-perturbation problems on coarse meshes. The setting is a high-order, discontinuous finite-element discretization, which allows for element-local basis enrichment. Near-wall basis functions augment the standard polynomial on elements adjacent to walls, where singular perturbations occur for high Reynolds number flows, to allow for the resolution of the state in the thin boundary layer. These functions consist of exponentially-scaled polynomials that are primarily active in the near-wall region. This approach obviates the need for highly-anisotropic elements, which are difficult to generate robustly for high-order discretizations on curved geometries. It also improves efficiency of the mesh, which can now consist of fewer elements, as additional elements required to make the transition between the near-wall and far-wall regions are eliminated. We demonstrate the approach for the solution of a one-dimensional scalar advection-diffusion-source problem and the representation of a Reynolds-averaged Navier-Stokes solution in two dimensions. The results show that at high Péclét and Reynolds numbers on coarse meshes, the augmented basis solution resolves the boundary layer much more accurately than standard polynomial approximation.

I. Introduction

Solutions to singular perturbation problems pose meshing challenges in multiple dimensions due to their highly-disparate length scales and high levels of anisotropy. An example is high-Reynolds number viscous flows, which are characterized by thin boundary layers near walls, in which the solution changes rapidly to meet a no slip velocity boundary condition. Efficient meshes for the resolution of such problems must typically exhibit similar anisotropy. With ideal element aspect ratios reaching $O(1000)$ for practical aerospace external flow applications, not taking advantage of the anisotropy can have a huge effect on the mesh size and computational cost. However, the generation of these meshes is difficult to automate, especially for high-order approximations on curved geometries, where large curved elements have a propensity to self-intersect and create negative Jacobians.

Much work already exists on curved mesh generation for high-order discretizations [1–5]. Yet this process is still not sufficiently robust in three dimensions, at the high anisotropy levels to be used for automated adaptation. Even when possible and successful, the meshes obtained for singular perturbation problems, such as flows governed by the Reynolds-averaged Navier-Stokes (RANS) equations, are still not necessarily efficient. The lack of efficiency comes from practical limitations on mesh conformity and size changes, and from the nature of the mesh generation algorithms. Whereas large anisotropy is required near walls, outside the boundary layer, isotropic elements suffice. It is this transition from anisotropy to isotropy, generally driven by mesh size change limits, that is often wasteful in degrees of freedom. Figure 1 shows an example mesh automatically generated using BAMG [6], using an output-based mesh optimization procedure [7], for flow over an MDA 30P30N high-lift airfoil at Mach number $M = 0.2$, Reynolds number $Re = 5 \times 10^6$, and angle of attack $\alpha = 10^\circ$. The solution approximation order is $p = 2$, and the geometry is represented using curved elements of order $q = 3$. Note the high anisotropy near the wall and the large number of elements needed to transition the mesh to more isotropic elements.

We present an alternative meshing an approximation approach to RANS problems using isotropic elements. The context of our work is a high-order discontinuous finite-element method [7–9], which permits local basis enrichment on individual elements, independently of neighboring elements. To resolve the boundary layer near the wall, we augment the standard polynomial approximation space with near-wall basis functions. These near-wall functions consist of polynomials scaled by a decaying exponential. The method requires modifications to quadrature rules and storage and evaluation of basis functions on elements adjacent to walls. However, it does not require curved anisotropic meshes, which greatly simplifies mesh generation.

*Professor, Department of Aerospace Engineering, AIAA Associate Fellow.

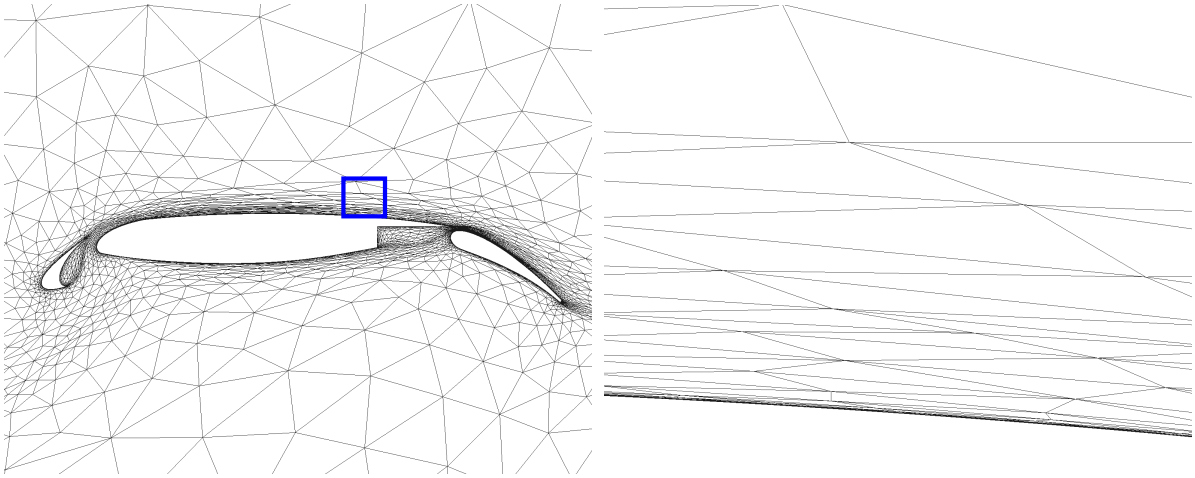

(a) airfoil and zoom box (b) mesh in the zoom box

Fig. 1 An adapted RANS mesh for a high-lift airfoil, MDA 30P30N, showing the large number of elements required to transition from high anisotropy in the boundary layer to more isotropic elements outside it. The nearly indiscernible mesh bunching near the wall consists of about 12 elements near the boundary layer.

The remainder of this paper presents motivating examples in Section II, describes the discontinuous Galerkin discretization in Section III, outlines the basis augmentation approach in Section IV, and presents results in Section V. Section VI concludes with a summary discussion.

II. Motivation

The premise of this work is that automated mesh generators often create too many elements when resolving high-Reynolds number flows. In support of this idea, we consider the MDA 30P30N airfoil from Figure 1. Taking a line probe through the middle of the zoom box, perpendicular to the surface, yields the velocity profile shown in Figure 2.

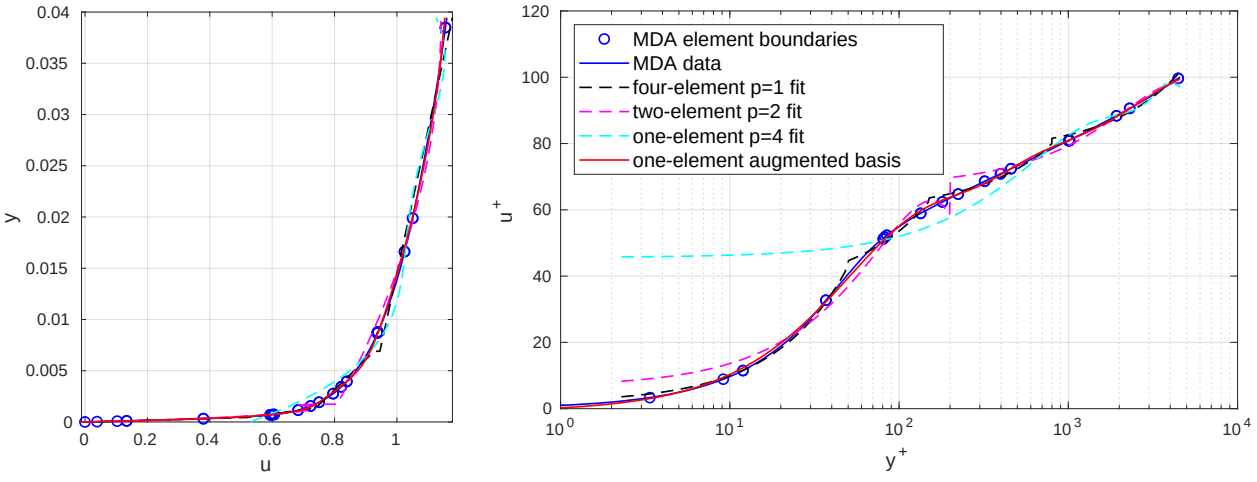

(a) CFD units (b) wall units

Fig. 2 Velocity profiles from a line-out of the MDA 30P30N airfoil data and fits using polynomials on discontinuous elements and the proposed augmented basis on one element.

This figure shows the velocity profile up to a wall-normal distance of $y \approx 0.04$, where for reference, the chord length of the main element is $c = 0.55$. The freestream speed is $u_\infty = 1$ in convenient "CFD units". In this line probe, there

are about 14 elements in the CFD mesh. Circles denote the element boundaries, and in each element the solution is approximated by $p = 2$ polynomials. The conservative variables are actually the ones approximated, but since the flow is low speed, density variations are small, so the velocity on each element is nearly quadratic too*.

Figure 2 also shows the same velocity profile in wall units, on a semi-log scale, so that the viscous sublayer and buffer layer are more clear. The edge of the profile corresponds to $y^+ \approx 4000$. We now ask: can we use fewer elements to approximate the same solution? The plot shows velocities obtained by least-squares projection using orders $p = 4, 2, 1$ on $1, 2, 4$ elements, respectively. Our goal is to dispense with the high anisotropy, and hence $O(1)$ elements in this vertical range is reasonable.

One $p = 4$ element does not do well, as it misses the buffer layer and the sublayer. Two elements at $p = 2$ are better, but the error is still high in the sublayer and the interface between elements at the start of the log layer. Four $p = 1$ elements does even better, showing that h-refinement is more efficient at this resolution. Note, the elements are not uniformly spaced – the interfaces were manually adjusted to minimize the L_2 error.

Figure 2 also shows the basis augmentation result, which is the topic of this paper. We use just one element at nominally $p = 2$ approximation, but we augment this basis with additional near-wall basis functions, which are $p = 2$ with an exponential damping, $\exp(-y/d_0)$, where d_0 is 200 wall units in this case. We see that this element is able to very well approximate the entire velocity profile. The caveats are that the integration must be modified to handle the new basis, and that the basis function representation has to be well conditioned. We address these points in the present paper.

III. Discretization

We present the basis function augmentation approach in the context of a discontinuous Galerkin (DG) finite-element spatial discretization. Consider a general conservation law given by the partial differential equation (PDE)

$$\partial_t \mathbf{u} + \partial_i \mathbf{F}_i(\mathbf{u}, \nabla\mathbf{u}) + \mathbf{S}(\mathbf{u}, \nabla\mathbf{u}) = \mathbf{0}, \tag{1}$$

where $\mathbf{u} \in \mathbb{R}^s$ is the state vector, $\mathbf{F}_i \in \mathbb{R}^s$ is the i^{th} component of the total flux, $1 \le i \le \text{dim}$ indexes the spatial dimension, dim, summation is implied on the repeated index i, and $\mathbf{S} \in \mathbb{R}^s$ is a source term. The total flux consists of convective and diffusive parts,

$$\mathbf{F}_i = \mathbf{F}_i^{\text{inv}}(\mathbf{u}) + \mathbf{F}_i^{\text{visc}}(\mathbf{u}, \nabla\mathbf{u}), \quad \mathbf{F}_i^{\text{visc}}(\mathbf{u}, \nabla\mathbf{u}) = -\mathbf{K}_{ij}(\mathbf{u})\, \partial_j \mathbf{u}, \tag{2}$$

where $\mathbf{F}_i^{\text{inv}} \in \mathbb{R}^s$ is the i^{th} component of the inviscid/convective flux, $\mathbf{F}_i^{\text{visc}} \in \mathbb{R}^s$ is the i^{th} component of the viscous flux, and $\mathbf{K}_{ij} \in \mathbb{R}^{s\times s}$ is the (i, j) component of the viscous diffusivity tensor. We will focus on steady problems, so that $\partial_t \mathbf{u} = \mathbf{0}$.

In DG, the state $\mathbf{u}$ is spatially approximated in functional form, using linear combinations of basis functions, usually polynomials, on each element. No continuity constraints are imposed on the approximations on adjacent elements. Denoting by T_h the set of N_e elements in a non-overlapping tessellation of the domain Ω, the state approximation becomes

$$\mathbf{u}_h(\vec{x}) \approx \sum_{e=1}^{N} \sum_{n=1}^{N_{be}} \mathbf{U}_{en} \phi_{en}(\vec{x}), \tag{3}$$

where N_{be} is the number of basis functions on element e, $\phi_{en}(\vec{x})$ is the n^{th} basis function on element e, and $\mathbf{U}_{en}$ is the vector of s coefficients on the n^{th} basis function on element e. We denote by $\mathcal{V}_h$ the solution approximation space, given by the span of the basis functions.

Multiplying the PDE in Eqn. 1 by test functions in the same space, $\mathbf{v}_h \in \mathcal{V}_h$, and integrating by parts gives the weak form associated with each element,

$$\mathcal{R}_h(\mathbf{u}_h, \mathbf{v}_h|_{\Omega_e}) = \int_{\Omega_e} \mathbf{v}_h^T \partial_t \mathbf{u}_h \, d\Omega - \int_{\Omega_e} \partial_i \mathbf{v}_h^T \mathbf{F}_i \, d\Omega + \int_{\partial\Omega_e} \mathbf{v}_h^{+T} \widehat{\mathbf{F}} \, ds - \int_{\partial\Omega_e} \partial_i \mathbf{v}_h^{+T} \mathbf{K}_{ij}^+ \left(\mathbf{u}_h^+ - \widehat{\mathbf{u}}_h\right) n_j \, ds, \tag{4}$$

where $(\cdot)^T$ denotes transpose, and on the element boundary $\partial\Omega_e$, the notations $(\cdot)^+$, $(\cdot)^-$ denote quantities taken from the element interior/exterior, respectively. The convective flux $\widehat{\mathbf{F}}^{\text{inv}}$ is computed using the Roe approximate Riemann solver [11], and the viscous flux is computed using the second form of Bassi and Rebay (BR2) [12].

*To be precise, the solution is quadratic in the reference space of each element, so that for the curved elements near the wall, the global state approximation is not precisely quadratic [10].

Using the approximation basis functions as the test functions gives the semi-discrete form

$$\mathbf{M}\frac{d\mathbf{U}}{dt} + \mathbf{R}(\mathbf{U}) = \mathbf{0}, \tag{5}$$

where $\mathbf{U} \in \mathbb{R}^{N_u}$ is the complete discrete state vector, N_u is the total number of unknowns including the state rank, $\mathbf{R}(\cdot) \in \mathbb{R}^{N_u}$ is the nonlinear spatial residual, and $\mathbf{M} \in \mathbb{R}^{N_u \times N_u}$ is the block-element sparse mass matrix. For steady simulations, the time derivative term drops out, although pseudo-time continuation remains in the solver to drive the steady residual to zero [13]. For nonlinear problems, the solver consists of a Newton-Raphson method with the generalized minimum residual (GMRES) [14] linear solver, preconditioned by an incomplete lower-upper factorization or an element-line Jacobi solver.

IV. Basis Augmentation

The idea of using non-polynomial basis functions to construct the approximation space of a discontinuous-Galerkin discretization has been investigated before [15, 16]. The goal of such work has been to customize the basis for the equation or boundary/initial conditions being solved, by replacing polynomials with trigonometric, exponential, or other types of functions. In this work, we take a general approach in which we keep the standard polynomial basis functions over all elements but then augment them with additional functions that provide more resolution on boundaries of elements adjacent to domain boundaries that exhibit singular-perturbation solutions, i.e. boundary layers. A similar process could be applied to the resolution of features such as thin wakes or even shocks, but these pose additional challenges and are outside of the scope of this initial study.

A. One Dimension

In singularly-perturbed problems, the solution exhibits a boundary layer behavior, in which the state u changes rapidly on a boundary to satisfy a given condition, such as no-slip for a high Reynolds number flow. Using a standard polynomial basis, e.g. Lagrange functions, resolution of the boundary layer takes small elements and/or high order. We therefore present a basis augmentation approach that more efficiently resolves the solution. This augmentation affects the element containing the boundary layer, which in one dimension will be on either the left or right side of the domain. In the following exposition, we present the approach for an element needing boundary-layer resolution on its left side. The reference element can be flipped to obtain the equivalent resolution increase on the right side.

Consider a reference element, $\xi \in [0, 1]$, with basis functions $\phi_i(\xi)$, $i = 1 \ldots n_p$, $n_p = p + 1$, that approximate a space of order p polynomials. We define an additional set of n_p *near-wall* basis functions, $\phi_i^*(\xi)$, $n = 1 \ldots n_p$ given by

$$\phi_n^*(\xi) = \phi_n(\xi^*)e^{-\xi/\xi_0}, \quad \xi^* \equiv \xi/\xi_0, \tag{6}$$

where $0 < \xi_0 < 1$ is a to-be-optimized parameter that correlates with the boundary-layer thickness. The additional coordinate ξ^* is defined to improve the conditioning of the near-wall basis: if $\xi^* = \xi$, many of the near-wall basis functions would look similar, especially at high order, p.

Figure 3 shows the original and near-wall basis for $p = 2$. Both sets of basis functions are used together to approximate the solution, so that an augmented element has $2n_p$ basis functions. The approximation space is no longer just polynomial, as it also contains exponentially-scaled polynomials biased towards one side. These additional functions allow for an efficient resolution of the boundary layer.

The augmented solution approximation is smooth inside an element, but the allowance for high variation on one side complicates integration via quadrature. Standard quadrature rules are generally derived for polynomial functions, and hence a large number of points would be required to accurately capture the near-wall variation. This inefficiency can be mitigated by modifying the integration rules. Various approaches are possible, and presently we consider a simple one: piece-wise integration. Specifically, we split the element into two sub-elements, $[0, \xi_0]$ and $[\xi_0, 1]$, and integrate on each one with separate quadrature. The reasoning for this split is that the near-wall basis is mostly active in the first sub-element, and its variations there are not relatively larger than the standard basis, which is active mostly in the second sub-element. Separate quadrature rules therefore sufficiently sample both sets of basis functions.

B. Two Dimensions

In two or more dimensions, we have more directions to consider and prospects of supporting general element types, e.g. triangles and quadrilaterals in two dimensions. We could extend the one-dimensional technique for constructing

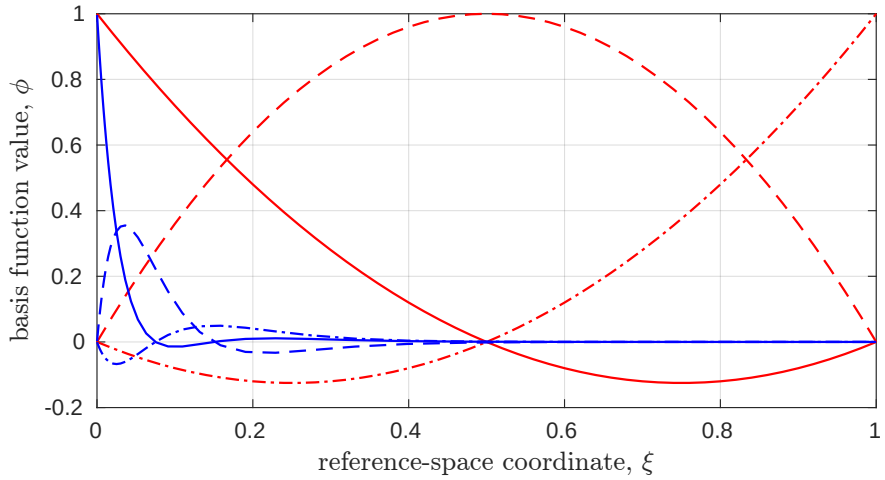

Fig. 3 Original (red) and additional near-wall (blue) basis functions based on $p = 2$ Lagrange polynomials on a reference element, $\xi \in [0, 1]$, obtained using Eqn. 6 with $\xi_0 = 0.05$. The near-wall functions are active on the left side and decay to near zero on the rest of the element.

augmented basis functions by identifying directions normal to walls and applying Eqn. 6 in those directions. Such a procedure could become cumbersome if rotations of reference coordinates were required to align with these normal directions, a likely scenario on general unstructured meshes where some elements may only have a node or edge on a boundary.

Therefore, in this work we propose an alternative basis function augmentation procedure that is based on the wall distance. The distance to the closest wall is already available in many CFD codes, as it is required for some turbulence models. Our goal is to use the wall distance to construct basis functions with high variation near the wall, ideally without modifying the existing, baseline, basis function evaluation procedure. One way to do this is to multiply the baseline basis functions by an exponential that depends on the wall distance,

$$\phi_n^*(\vec{\xi}) = \phi_n(\vec{\xi}) e^{-d(\vec{\xi})/d_0}, \tag{7}$$

where $d(\vec{\xi})$ is the wall distance at reference coordinate $\vec{\xi}$ in the mesh, and d_0 is an element-specific distance parameter that measures the boundary-layer thickness. This parameter would be optimized as part of mesh adaptation and optimization.

As defined in Eqn. 7, the basis functions will be come ill-conditioned as the order increases and/or d_0 decreases – for example, if using standard Lagrange functions, many of the functions will be zero on an element boundary. We therefore use a modified Gram-Schmidt orthonormalization to improve conditioning. This is done in two steps. First, we remove components of the original basis from the new basis,

$$\text{for } i = 1 : n_p, \quad \text{for } j = 1 : n_p, \quad \phi_j^* = \phi_j^* - \frac{(\phi_i, \phi_j^*)}{(\phi_i, \phi_i)} \phi_i,$$

where the inner product $(\cdot, \cdot)$ is a reference-space integration. Second, we orthonormalize the augmented basis functions,

$$\text{for } i = 1 : n_p, \quad \left\{ \phi_i^* = \frac{\phi_i^*}{(\phi_i^*, \phi_i^*)}, \quad \text{for } j = (i+1) : n_p, \quad \phi_j^* = \phi_j^* - (\phi_i^*, \phi_j^*) \phi_i^*, \right\}$$

In practice, the integrals are replaced with quadrature, and we work with basis functions evaluated at quadrature points. The quadrature rules can be efficiently obtained by splitting the element into near-wall and remaining regions based on the wall-distance. For the present proof-of-concept study, a very high-order quadrature rule is used instead.

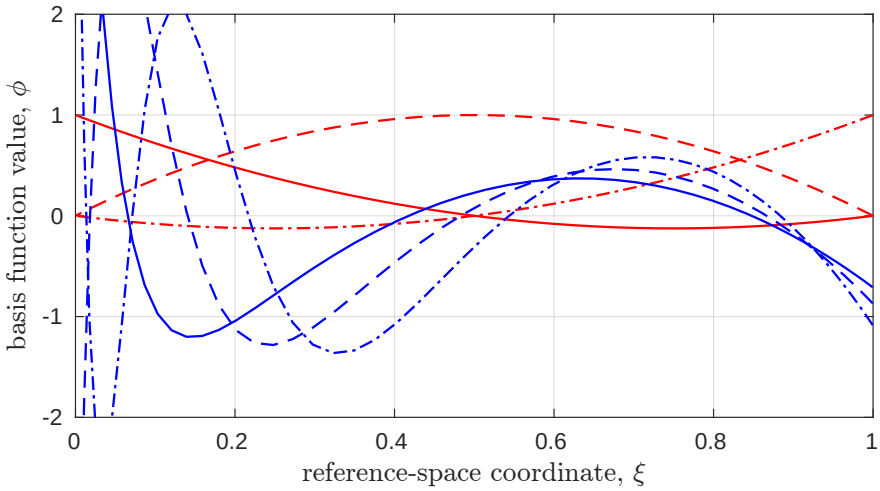

Fig. 4 Original (red) and additional near-wall (blue) basis functions based on $p = 2$ Lagrange polynomials on a reference element, $\xi \in [0, 1]$, obtained using Eqn. 7 with $d_0 = 0.05$. The reference element is assumed to map to a unit element in global coordinates.

V. Results

A. Scalar Transport

We first present the proposed basis augmentation approach for a steady one-dimensional scalar advection-diffusion equation with a source term,

$$au_x - \nu u_{xx} + s(x) = 0, \quad x \in [0, L], \quad u(0) = u(L) = 0, \tag{8}$$

where for the examples below, $L = 1$, $a = 1$, and $s(x) = 2\sin(\pi x/L)$. The Péclét number is defined as $\mathrm{Pe} \equiv aL/\nu$.

For high Péclét numbers, the solution to Eqn. 8 exhibits a singular perturbation on the right boundary, resulting in a boundary layer in which u drops rapidly to satisfy the boundary condition. This boundary layer can be better resolved using an appropriately chosen augmented basis on the right-most element.

We demonstrate the utility of the augmented basis by comparing discontinuous-Galerkin solutions to Eqn. 8 using both a standard and an augmented basis, at various orders, p. First, Figure 5 shows solutions at three orders, $p = 2, 3, 4$ for $N = 8$ elements using a standard polynomial approximation space on each element. We see oscillations on the right-most element, which contains the boundary layer where the solution must change rapidly to meet the $u = 0$ boundary condition on the right. Only $p = 4$ at $\mathrm{Pe} = 100$ shows signs of adequate resolution, while at $\mathrm{Pe} = 1000$ all solutions are oscillatory. Note, the boundary layer thickness is $\delta \sim L/\mathrm{Pe}$, which at $\mathrm{Pe} = 1000$ is much smaller than the effective resolution, $\Delta x/p = L/(Np)$, when $N = 8$, $p = 4$.

We now consider using an augmented basis, with near-wall basis functions added to the right-most element, on its right side. We set the ξ_0 parameter in Eqn. 6 based on the boundary layer thickness, $\xi_0 = \delta/\Delta x = (L/\mathrm{Pe})/(L/N) = N/\mathrm{Pe}$. Figure 6 shows the DG solutions obtained using the augmented basis, for $N = 8$ elements and nominal approximation orders $p = 1, 2, 3, 4$. We see no oscillations in any of the results, and much lower L_2 error values, computed relative to a very fine resolution simulation, compared to the standard polynomial approximation.

Figure 7 shows the L_2 error convergence results for the cases tested. For each order and basis type, simulations were run with different mesh sizes, N. The L_2 error was then computed relative to a very fine solution, and the convergence was plotted versus the number of degrees of freedom. Using degrees of freedom accounts, albeit in a rudimentary way, for the higher cost of higher order and basis-function augmentation.

From the results in the figure, we see that the standard basis of polynomials on each element exhibits slow convergence, which is expected because of the poor resolution of the boundary layer. Small elements are needed to resolve this layer well, and with uniform refinement, many elements are required. At $\mathrm{Pe} = 1000$, the standard basis results show almost no improvement in the L_2 error over the range of N values tested.

On the other hand, the augmented basis results show much better convergence, even on coarse meshes. For these results, we start with a very coarse mesh of only 2 elements. At the highest order of $p = 4$ on this mesh, the L_2 error

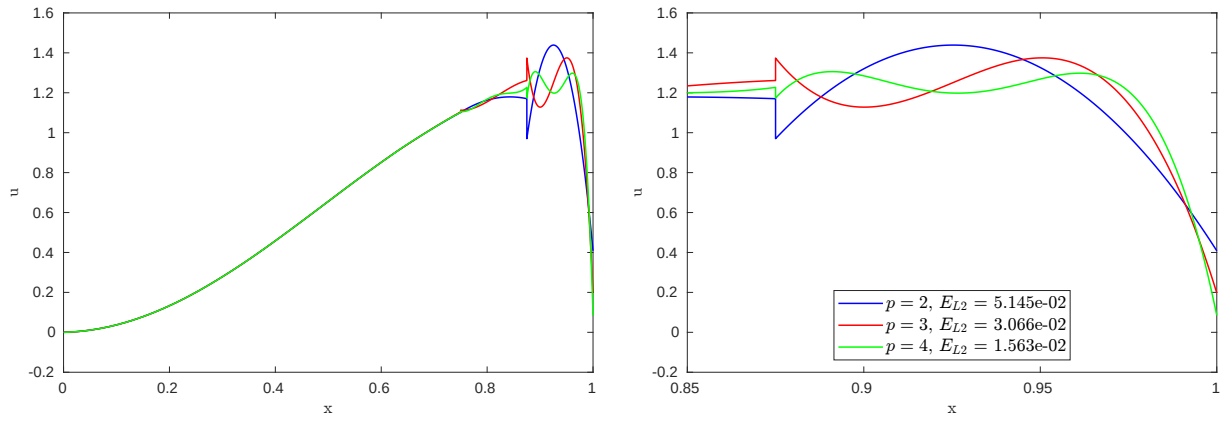

(a) Pe = 100 (b) Pe = 100 (zoom)

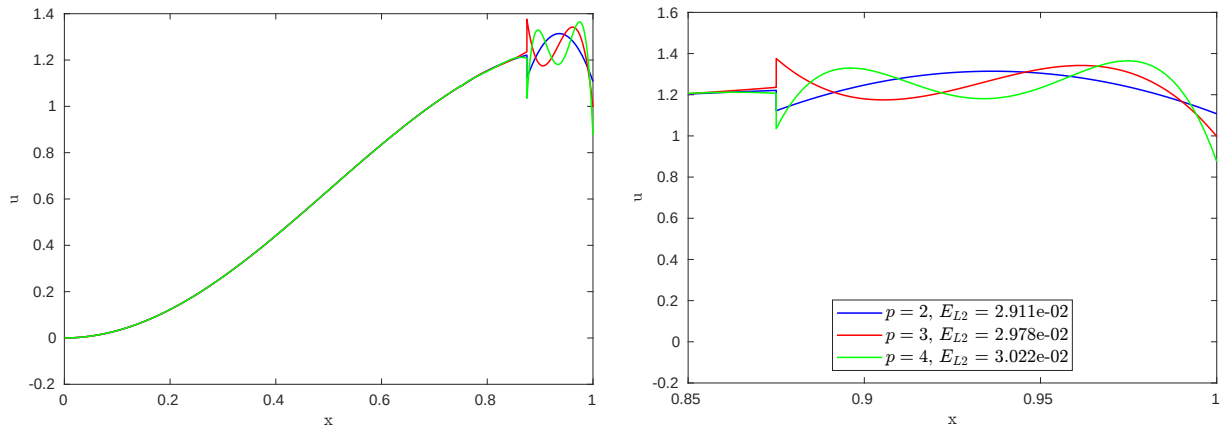

(c) Pe = 1000 (d) Pe = 1000 (zoom)

Fig. 5 DG solutions to the scalar advection-diffusion-source equation on $N = 8$ elements using a standard polynomial approximation space.

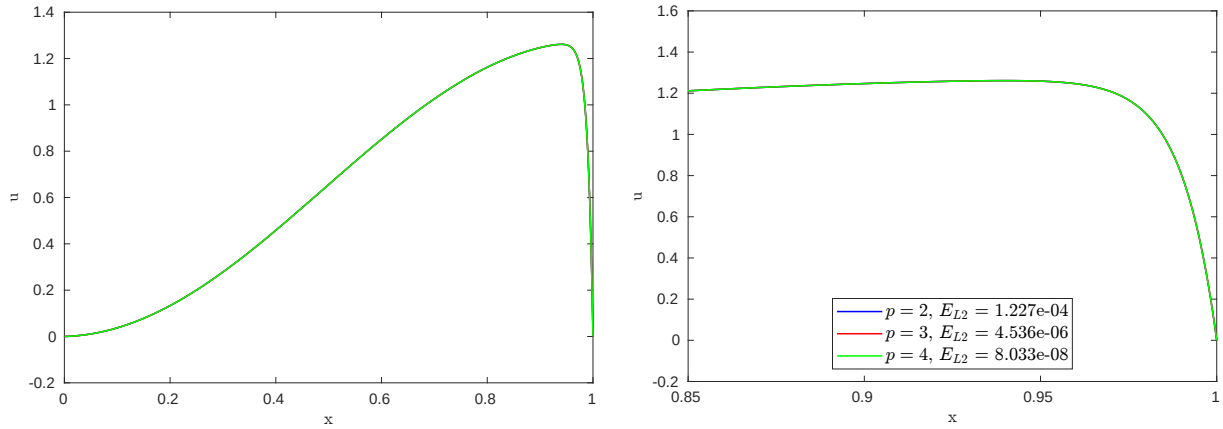

(a) Pe = 100 (b) Pe = 100 (zoom)

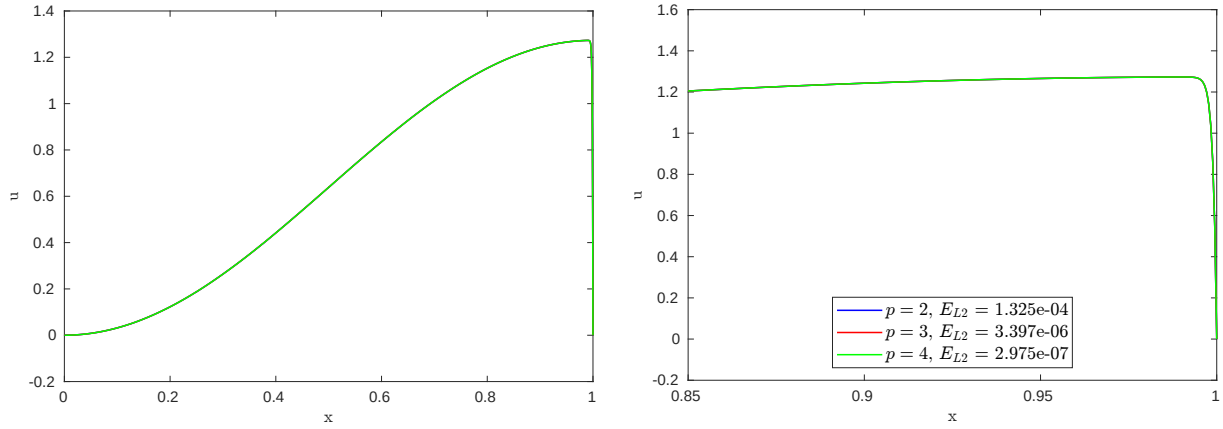

(c) Pe = 1000 (d) Pe = 1000 (zoom)

Fig. 6 DG solutions to the scalar advection-diffusion-source equation on $N = 8$ elements using a polynomial approximation space augmented with near-wall basis functions on the right-most element.

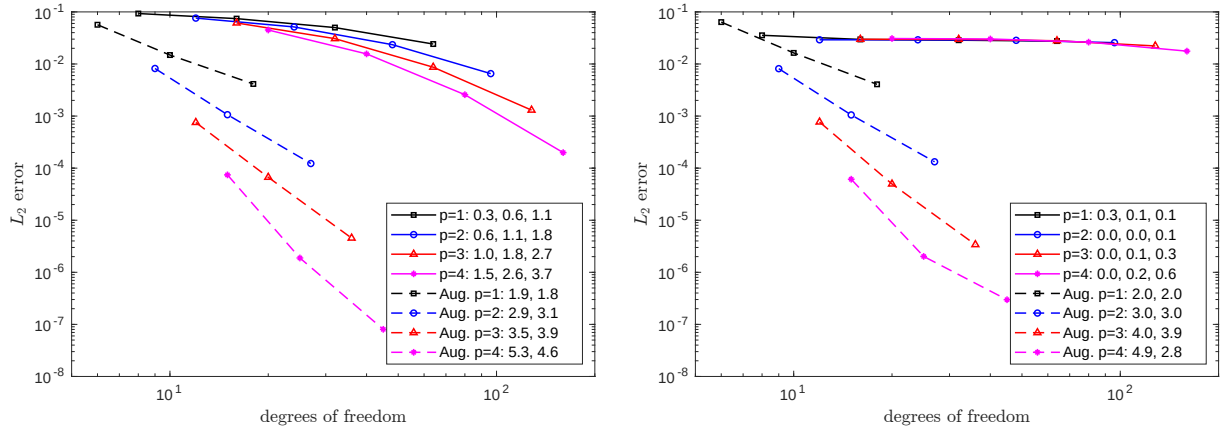

(a) Pe = 100 (b) Pe = 1000

Fig. 7 L_2 error norm convergence plots for standard and augmented basis functions, at various p and for the two Péclét numbers.

is lower than any of the standard basis results on finer meshes. Furthermore, in the legends, the figure also shows slopes at each segment between data points. We see that the augmented basis achieves the expected $p+1$ error in most cases, whereas the standard basis struggles to reduce the error, even at the finest meshes. This is clearly evident in the Pe = 1000 case.

B. Reynolds-Averaged Navier-Stokes

For a two-dimensional example, we consider turbulent flow over a NACA 0012 airfoil at $M = 0.25$ and $Re = 10^4$. The Reynolds-averaged Navier-Stokes equations are solved using the Spalart-Allmaras turbulence model [17, 18]. Details on the discontinuous Galerkin discretization and solver can be found in previous works [19, 20].

A coarse quadrilateral mesh, a closeup of which is shown in Figure 8(a), is used for this study. The wall is an adiabatic no-slip boundary condition, and the farfield is approximately 100 chord lengths away from the airfoil. The elements are curved via a $Q = 3$ order mapping from reference space, and Lagrange basis functions on Gauss points are used for the solution approximation space. At order p, there are $n_p = (p+1)^2$ basis functions, and these are used to independently approximate the five components of the conservative state vector, $\mathbf{u} = [\rho, \rho u, \rho v, \rho E, \rho\tilde{\nu}]^T$.

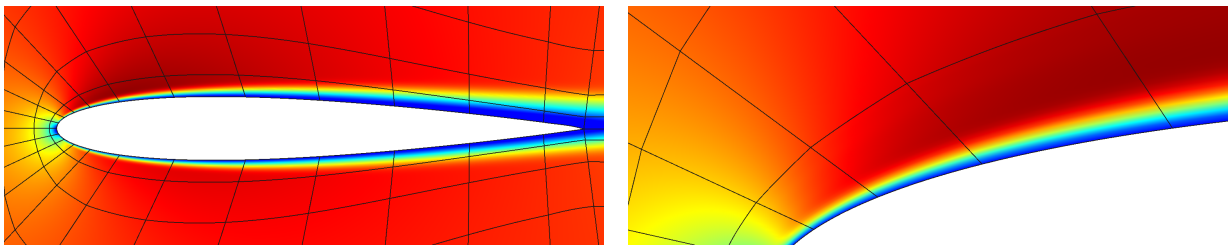

(a) airfoil view (b) upper leading-edge zoom

Fig. 8 x-momentum contours for a $p = 9$ "truth" DG solution to the RANS equations.

Figure 8 shows the x-momentum contours for this case. The boundary layer develops on both sides of the airfoil and grows in thickness from the leading to trailing edge. The mesh elements adjacent to the wall are not designed to capture the anisotropic boundary layer. Particularly for the elements near the leading edge, most of the velocity variation occurs in the first 10-20% of the element near the wall. At low and moderate orders, standard polynomial approximation fails to capture the capture this variation accurately. Our goal is to show that, in contrast, an augmented basis is capable of approximating the boundary layer even at low orders.

Unlike in the one-dimensional example, in this case, the augmented basis is not yet integrated into the solver. Instead, to gauge the benefits of using an augmented basis, a high-order ($p = 9$) "truth" solution is projected down, in a least-squares sense, to various approximation spaces and errors are computed relative to the truth solution. If $\mathbf{U}_h \in \mathbb{R}^{n_h}$ denotes the coefficients in the fine-space truth approximation on one element e, using basis functions ϕ_h, then the coefficients, $\mathbf{U}_H$, in a coarse-space approximation using basis functions ϕ_H on the same element are given by

$$\mathbf{U}_H = \mathbf{M}_H^{-1}\mathbf{N}_{Hh}\mathbf{U}_h, \quad M_{H,ij} \equiv \int_{\Omega_e} \phi_{H,i}\phi_{H,j}\, d\Omega, \quad N_{Hh,ij} \equiv \int_{\Omega_e} \phi_{H,i}\phi_{h,j}\, d\Omega, \tag{9}$$

Coefficients associated with different state components are projected independently. The projection is performed only on the elements adjacent to the boundary, the set of which is denoted by Q_b.

Figure 9 shows the contours for the projections to $p = 1$ using the standard Lagrange basis and the augmented basis. Note, to visualize the solution using the augmented basis, the state is projected back to the truth approximation space, $p = 9$. We see that the standard basis $p = 1$ space cannot capture the boundary layer at all. There is some variation in the normal direction, which makes the velocity lower near the wall than further away from it, but this variation then causes an overshoot in the velocity further from the wall. In contrast, the augmented basis captures the boundary layer well: the velocity decreases to zero over a small extent near the wall, and the approximation away from the wall does not show any significant oscillations.

Next, we consider projection to $p = 2$. Figure 10 shows the x-momentum contours of the projections to the standard and augmented basis. For the standard $p = 2$ basis, the velocity gets closer to zero near the wall, at the cost of oscillations

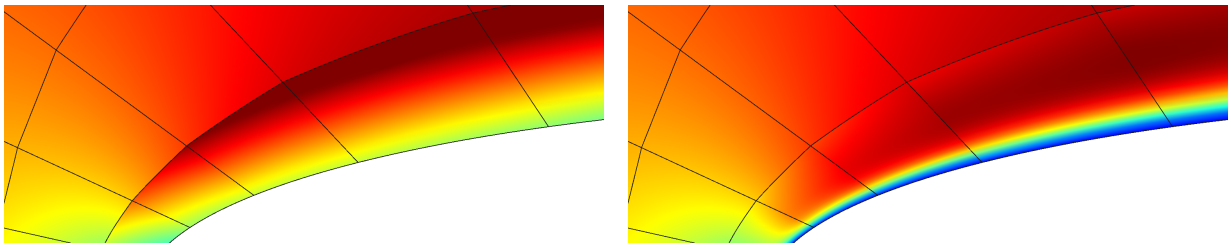

(a) standard basis (b) augmented basis

Fig. 9 x-momentum contours for $p = 1$ projections of the RANS solution.

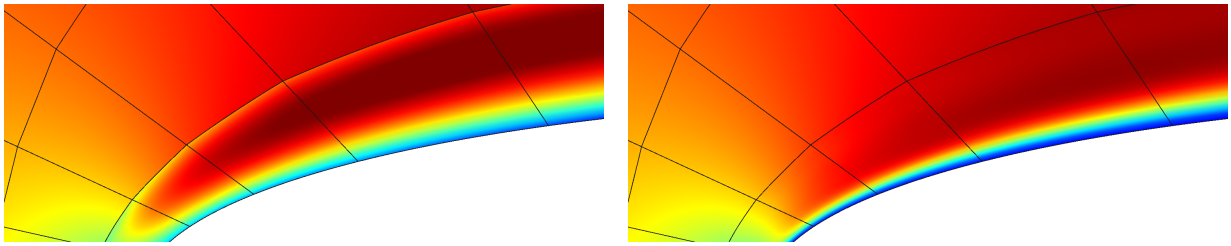

(a) standard basis (b) augmented basis

Fig. 10 x-momentum contours for $p = 2$ projections of the RANS solution.

further from the wall in the boundary elements. On the other hand, the $p = 2$ augmented basis captures the boundary layer very well: differences between the truth solution and the projection are imperceptible.

Finally, Figure 11 shows the projections for $p = 3$. The standard basis now exhibits a reasonably well-defined boundary layer, but oscillations persist away from the wall. On the other hand, the augmented basis $p = 3$ projection is again visually identical to the truth solution.

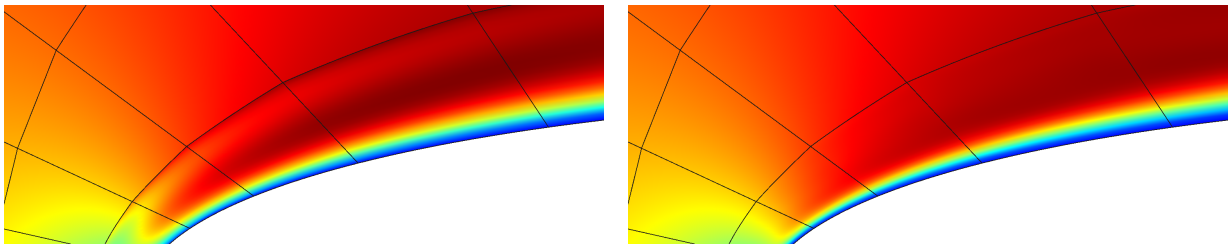

(a) standard basis (b) augmented basis

Fig. 11 x-momentum contours for $p = 3$ projections of the RANS solution.

For the augmented-basis projections, the value of d_0 in Eqn. 7 has to be chosen. The eventual goal in an online solver implementation is that this value will be optimized together with the mesh, e.g. in an output-based setting [7]. Presently, we implement a simple line-search on each element to determine the optimal value for the projection. Prior to the line search, a range of d_0 values is considered on a single element. Projections are performed, and the d_0 value that yields the projection with the lowest error is used as the starting point. The line search then adjusts this value to find the lowest-error projection.

The L_2 error in a projected solution is computed relative to the truth solution by summing the L_2 errors over the set of all boundary elements, Q_b,

$$E_{L2}^2 = \sum_{e \in Q_b} \int_e ||\mathbf{u} - \mathbf{u}_{\text{truth}}||^2 \, d\Omega. \tag{10}$$

Note that in this expression, the errors in all state components (mass, momentum, energy, $\tilde{\nu}$) are summed together. Table 1 presents the projection errors for $p = 1, 2, 3$. The greatest benefit is at $p = 1$, where the augmented basis yields an error that is almost 16 times lower than the standard basis. The benefit drops to a factor of 8 for $p = 2$ and a factor of 4 for $p = 3$ – still very good improvements in the approximation.

Table 1 State L_2 errors, E_{L2}, over boundary elements.

Order	Standard basis	Augmented basis
$p = 1$	2.91×10^{-2}	1.85×10^{-3}
$p = 2$	4.82×10^{-3}	6.42×10^{-4}
$p = 3$	1.25×10^{-3}	2.92×10^{-4}

For a better comparison of the velocity, Figure 12 shows the velocity profiles taken along a line normal to the airfoil on the upper surface at about 15% chord location from the leading edge. The upper limit on these plots is the extent of the boundary element, so that all of the variation seen in the figures occurs in one element. We observe the very poor performance of the $p = 1$ standard basis and the improvement with increasing order, albeit with oscillations remaining. The augmented basis, on the other hand, yields velocity profiles that conform very well to the truth solution. The velocity profile errors, computed as an L_2 norm relative to the truth solution and shown in the legends, quantify the benefits of the augmented basis: the error reduction factors range from 13 to 30.

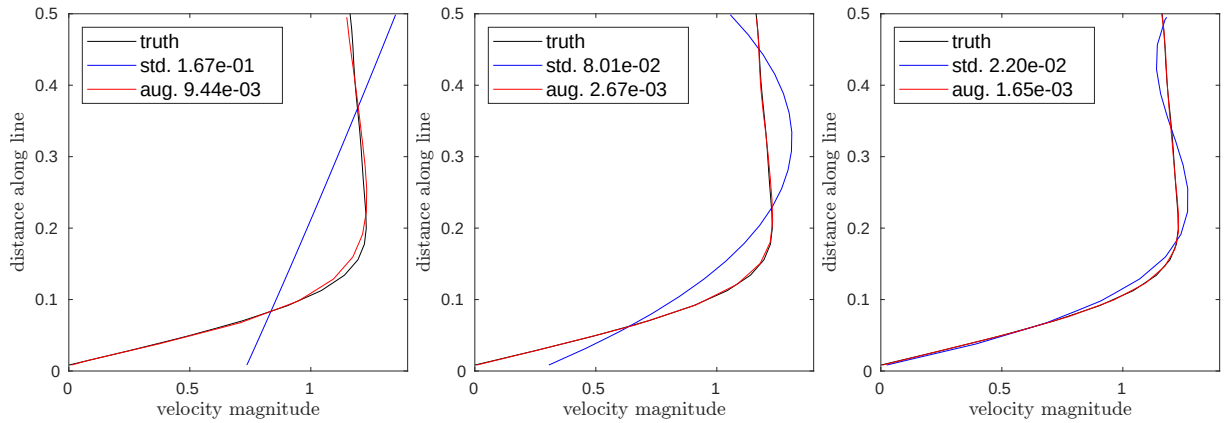

(a) $p = 1$ (b) $p = 2$ (c) $p = 3$

Fig. 12 Boundary-layer velocity profiles in a boundary element of the RANS case.

VI. Conclusions

This paper presents a technique for efficiently approximating solutions to singular-perturbation problems using customized near-wall basis functions. The context is a high-order discontinuous finite-element discretization, which allows for element-independent approximation space enrichment. Elements adjacent to walls where boundary conditions cause singular perturbations, such as no-slip in a high-Reynolds number flow, receive extra basis functions that are active in the boundary layer, to allow them to approximate the boundary-layer solution. These additional basis functions relieve difficulties and inefficiencies associated with using very small mesh elements to resolve the boundary layer. The meshing difficulty arises from maintaining positive element Jacobians on highly-anisotropic curved elements, which are needed for high-order discretizations. The inefficiency of using small elements comes from practical meshing constraints, which generally lead to limits on the maximum size changes and hence gradual changes in size and stretching that increase the total element count.

The results in this paper demonstrate the proposed basis enrichment approach on a one-dimensional scalar advection-diffusion-source problem, and on a two-dimensional Reynolds-averaged Navier-Stokes problem. For the one-dimensional

problem, at high Péclét numbers, the augmented-basis solutions show much lower errors than the standard polynomial basis solutions, and they allow for resolution of the boundary layer even on very coarse meshes. The L_2 error reduction factor compared to using a standard basis ranges from 2 to almost 6 orders of magnitude, for the orders and Péclét number tested. A convergence study on uniform meshes then yields optimal rates even on coarse meshes when using the augmented basis. In contrast, at the high Péclét number of 1000, the standard basis shows barely any signs of convergence, even up to 128 elements at $p = 4$, the error being dominated by the boundary element with the singular perturbation.

The 2D RANS case is a proof of concept demonstration, as the augmented basis is not yet implemented into the solver. Instead, the benefits of the augmentation are assessed by projecting a fine-space truth solution to both standard and augmented approximation spaces at orders $p = 1, 2, 3$. The resulting projected solutions show that, as expected, the augmented basis is able to capture the boundary layer very well, especially at low orders, for which the standard basis struggles to satisfy the boundary conditions without overshoots or oscillations in the rest of the element.

Several practicalities remain to be addressed to make this method viable. First comes the question of integration. Standard quadrature rules in a coarse element, at least at reasonable integration orders, will not adequately sample the large variation in the singular-perturbation region. Options include deriving customized quadrature rules, e.g. using a stretching transformation, or subdividing the element into two pieces, a near-wall region and the rest, and using standard quadrature rules on each piece. The latter option was used effectively in one dimension but has not yet been tried in two dimensions. Another practicality is the selection of the singular perturbation region thickness, d_0, an optimal value of which exists for a particular solution to make the approximation the most accurate. We envision the selection of d_0 occurring concurrently with solution-based mesh optimization.

Additional variations in the algorithms can likely further improve efficiency. One of these is using different values of d_0 for different state components, some of which may not show as much variation near the boundary, or variation on a different length scale (for example, the eddy viscosity versus the velocity in a RANS calculation). Another efficiency improvement may come from lower-order enrichment. For example, $p = 1$ or $p = 2$ augmented basis functions could be sufficient for enriching a higher-order baseline approximation.

The present augmentation approach targets singular perturbations at boundaries. This allows for the use of the wall distance function, already needed in some turbulence models, to define the new basis. Applying the same approach to the resolution of shear layers and shocks would be complicated by the need to define a distance to these singular features. In addition, these features do not typically present as much difficulty in meshing, since they do not need to be curved like geometry boundaries. Our future work will therefore likely focus on wall-induced singular perturbations, particularly at high Reynolds numbers, which will further stress the conditioning and integration.

References

[1] Persson, P.-O., and Peraire, J., "Curved mesh generation and mesh refinement using Lagrangian solid mechanics," AIAA Paper 2009-0949, 2009. https://doi.org/https://doi.org/10.2514/6.2009-949.

[2] Geuzaine, C., Johnen, A., Jonathan Lambrechts, J., Remacle, J.-F., and Toulorge, T., "The generation of valid curvilinear meshes," *IDIHOM: industrialization of high-order methods-a top-down approach*, Springer, 2015, pp. 15–39. https://doi.org/10.1007/978-3-319-12886-3_2.

[3] Abgrall, R., Dobrzynski, C., and Froehly, A., "A method for computing curved meshes via the linear elasticity analogy, application to fluid dynamics problems," *International Journal for Numerical Methods in Fluids*, Vol. 76, No. 4, 2014, pp. 246–266. https://doi.org/10.1002/fld.3932.

[4] Karman, S. L., Ervin, J., Glasby, R. S., and Stefanski, D. L., "High-order mesh curving using WCN mesh optimization," AIAA Paper 2016-3178, 2016. https://doi.org/10.2514/6.2016-3178.

[5] Ruiz-Gironés, E., Sarrate, J., and Roca, X., "Generation of curved high-order meshes with optimal quality and geometric accuracy," *Procedia engineering*, Vol. 163, 2016, pp. 315–327. https://doi.org/https://doi.org/10.1016/j.proeng.2016.11.108.

[6] Borouchaki, H., George, P., Hecht, F., Laug, P., and Saltel, E., "Mailleur bidimensionnel de Delaunay gouverné par une carte de métriques. Partie I: Algorithmes," INRIA-Rocquencourt, France. Tech Report No. 2741, 1995.

[7] Fidkowski, K. J., "A Local Sampling Approach to Anisotropic Metric-Based Mesh Optimization," AIAA Paper 2016–0835, 2016. https://doi.org/10.2514/6.2016-0835.

[8] Fidkowski, K. J., "Output error estimation strategies for discontinuous Galerkin discretizations of unsteady convection-dominated flows," *International Journal for Numerical Methods in Engineering*, Vol. 88, No. 12, 2011, pp. 1297–1322. https://doi.org/10.1002/nme.3224.

[9] Fidkowski, K. J., "An Output-Based Dynamic Order Refinement Strategy for Unsteady Aerodynamics," AIAA Paper 2012-77, 2012. https://doi.org/10.2514/6.2012-77.

[10] Sanjaya, D. P., and Fidkowski, K. J., "Improving High-Order Finite Element Approximation Through Geometrical Warping," AIAA Paper 2015–2605, 2015. https://doi.org/10.2514/6.2015-2605.

[11] Roe, P., "Approximate Riemann solvers, parameter vectors, and difference schemes," *Journal of Computational Physics*, Vol. 43, 1981, pp. 357–372. https://doi.org/https://doi.org/10.1016/0021-9991(81)90128-5.

[12] Bassi, F., and Rebay, S., "GMRES discontinuous Galerkin solution of the compressible Navier-Stokes equations," *Discontinuous Galerkin Methods: Theory, Computation and Applications*, edited by B. Cockburn, G. Karniadakis, and C.-W. Shu, Springer, Berlin, 2000, pp. 197–208. https://doi.org/10.1007/978-3-642-59721-3_14.

[13] Ceze, M. A., and Fidkowski, K. J., "Constrained pseudo-transient continuation," *International Journal for Numerical Methods in Engineering*, Vol. 102, 2015, pp. 1683–1703. https://doi.org/10.1002/nme.4858.

[14] Saad, Y., and Schultz, M. H., "GMRES: A Generalized Minimal Residual Algorithm for Solving Nonsymmetric Linear Systems," *SIAM Journal on Scientific Computing*, Vol. 7, No. 3, 1986, pp. 856–869. https://doi.org/https://doi.org/10.1137/0907058.

[15] Yuan, L., and Shu, C.-W., "Discontinuous Galerkin method based on non-polynomial approximation spaces," *Journal of Computational Physics*, Vol. 218, No. 1, 2006, pp. 295–323. https://doi.org/10.1016/j.jcp.2006.02.013.

[16] Lee, K., Choi, J.-I., and Yoon, J., "Improving the third-order WENO schemes by using exponential polynomial space with a locally optimized shape parameter," *Computers and Mathematics with Applications*, Vol. 149, 2023, pp. 24–37. https://doi.org/10.1016/j.camwa.2023.08.021.

[17] Spalart, P. R., and Allmaras, S. R., "A One-Equation Turbulence Model for Aerodynamic Flows," *La Recherche Aérospatiale*, , No. 1, 1994, pp. 5–21. https://doi.org/10.2514/6.1992-439.

[18] Allmaras, S., Johnson, F., and Spalart, P., "Modifications and Clarifications for the Implementation of the Spalart-Allmaras Turbulence Model," Seventh International Conference on Computational Fluid Dynamics (ICCFD7) 1902, 2012.

[19] Fidkowski, K. J., "Gradient-based shape optimization for unsteady turbulent simulations using field inversion and machine learning," *Aerospace Science and Technology*, Vol. 129, 2022, p. 107843. https://doi.org/https://doi.org/10.1016/j.ast.2022.107843.

[20] Fidkowski, K. J., and Ceze, M. A., "High-Order Output-Based Adaptive Simulations of Turbulent Flow Over a Three Dimensionsional Bump," AIAA Paper 2015–0862, 2016. https://doi.org/10.2514/6.2016-0862.